Engineering with Computers (2026) 42:21
https://doi.org/10.1007/s00366-025-02262-5

ORIGINAL ARTICLE

Bridging experiments and defects' mechanics: a data-driven toolbox for configurational force analysis

Abdalrhaman Koko[1,2] · Alya Abdelnour[3] · Thorsten H. Becker[4] · T. James Marrow[2]

Received: 20 May 2025 / Accepted: 16 October 2025

Abstract
Understanding the mechanical behaviour of defective materials is key to predicting failure and enhancing performance. Traditional fracture mechanics often requires assumptions about geometry and loading that are unavailable in experimental systems. We present a MATLAB-based computational toolbox that extracts configurational forces and mixed-mode SIFs directly from experimentally measured displacement or deformation gradient fields, like digital image/volume correlation and high (angular) resolution electron backscatter diffraction. The toolbox implements path-independent energy integrals, including the *J*- and *M*-integrals, and introduces a novel mode decomposition formulation that isolates mode I–III SIFs contributions without predefined specimen geometries, applied loads, or boundary conditions. Applications to microcracks, dislocations, and fatigue cracks demonstrate its robust, geometry-independent characterisation, which can enable data-driven analysis of defect behaviour in anisotropic and complex materials. The framework is material-agnostic in principle and operates directly on experimental fields; however, its current implementation assumes small-strain kinematics, making it most applicable to linear and anisotropic elastic and elastoplastic materials such as metals and ceramics.

Keywords Configurational forces · Stress intensity factors · Mixed-mode fracture · HR-EBSD · Digital image correlation · Computational toolbox; material testing 2.0

1 Introduction

When a force ($\overrightarrow{F}$) acts on a particle, causing it to move along a trajectory; the work (W) done by the force is given by the dot product of the force and the displacement vector ($\Delta\,\overrightarrow{r}$),

$$W = \overrightarrow{F}.\Delta\,\overrightarrow{r} \tag{1}$$

For more complex trajectories where the force varies, the work is calculated by integration along the particle's path (Γ), resulting in the integral form

$$W = \int_{\Gamma} \overrightarrow{F}.d\overrightarrow{r} \tag{2}$$

Thus, the work for a vector force field is calculated using a line integral. Additionally, the direction of the vector ($\overrightarrow{T}$) that is tangential to the trajectory over a small interval is represented by the arc element ds, so [1]

$$W = \int_{\Gamma} \overrightarrow{F}.\overrightarrow{T}ds \tag{3}$$

If the vector field is a gradient field ($\nabla\,\overrightarrow{F}$), it can be derived from a scalar potential function. In this case, the line integral between two points depends only on the endpoints and is independent of the path taken — the field is said to be conservative. For any closed path enclosing no source or sink, the line integral evaluates to zero. The scalar potential (or potential energy) associated with such a field describes

✉ Abdalrhaman Koko
abdo.koko@npl.co.uk

1 National Physical Laboratory, Hampton Road, Teddington TW11 0LW, UK

2 Department of Materials, University of Oxford, Oxford OX1 3PH, UK

3 Department of Mechanical Engineering, University of Khartoum, Khartoum, Sudan

4 Centre for Materials Engineering, Department of Mechanical Engineering, University of Cape Town, Cape Town, South Africa

Published online: 14 January 2026

the energy stored by the force field. This concept underpins the conservation of energy and momentum, as captured by Noether's theorem [2, 3], which states that path-independent integrals correspond to conserved physical quantities in systems with continuous symmetries. In solid mechanics, this principle forms the foundation for configurational force integrals used to describe defect mechanics.

In solid mechanics, surface traction in elastic bodies is described in terms of a vector field with respect to the surface's initial position. Since the body force density can be considered fixed in elastic bodies, the potential energy is a function of the displacement field [4, 5]. When evaluated over a surface that encloses a stress-concentrating defect, these conservation integrals represent a configurational force on the defect, which may be, for example, an inclusion [6] or dislocation [7, 8]. These integrals are direct consequences of momentum balance. The significance of these integrals in engineering and materials mechanics emerged as researchers sought to quantify the energy dissipation associated with material deformation, especially in the presence of defects. This force, defined as the negative gradient of the material's total energy with respect to the defect's position, diverges from traditional Newtonian mechanics by originating not from the material's physical position in space but rather from the defect's position within the structure [6, 7]. The configurational force was further elaborated through the development of the Peach-Koehler force [8], which describes the interaction between dislocations and stress fields generated by defects in the elastic medium. This theory was later refined via the divergence of Eshelby's stress tensor [9, 10], firmly establishing the role of these forces in classical dislocation theory [11].

A major milestone in the field of fracture mechanics came with Rice's formulation of the *J*-integral [12] as a path-independent integral to quantify the strain energy release rate during crack propagation. The *J*-integral allows for precise evaluations of strain energy dissipation in materials undergoing fracture, including anisotropic, linear, and nonlinear materials [4, 13]. The *J*-integral is central to modern fracture mechanics. It is easy to implement in finite element software, and has been coupled with residual stress, internal tractions, and thermal and electrochemical processes [14], and the analytical solutions for stress intensity factors used in standardised fracture toughness tests are either approximated or derived from the *J*-integral [15]. Further expansion of energy conservation principles led to the introduction of invariant integrals such as *M*-, and *L*-integrals [16, 17], generalising the *J*-integral to account for energy dissipation modes. These invariant integrals have been used to characterise the energy available for defect propagation or transformation [18–20], as they provide a descriptor of the deformation field at stress-concentrating defects, such as complex crack growth scenarios [21–24], dislocations [25, 26], inclusions [27], and slip bands [28].

Stress concentrations influence material failure, making understanding and quantifying how they affect the failure mechanisms is essential. Researchers, such as Lazar [29–31], extended the *J*-, *M*-, and *L*-integrals into gradient elasticity theory, applying them to inhomogeneous, incompatible, and anisotropic materials. These extensions are particularly relevant to materials containing dislocations and disclinations, since classical elasticity theory fails to describe their interactions at the micro-scale.

However, the invariant integrals do not distinguish between mechanical loading conditions (i.e., tensile and compressive mode I, in-plane shear mode II, and out-of-plane shear mode III) at the defects, which is crucial since it is well established in fracture mechanics that these conditions can affect both the defect growth rate and direction [32]. Traditionally, the mode I–III stress intensity factors (SIFs) have been obtained using analytical solutions [33, 34] or finite element methods (FEM), relying on known or idealised loads, boundary conditions, and specimen geometries [35, 36]. However, real-world conditions introduce uncertainties that undermine these approaches [37–39], such as residual stresses [40, 41], frictional effects [42], misalignment [43, 44], and the lack of knowledge of the boundary conditions. This complicates stress field characterisation, especially at the micro-scale where deformation is microstructurally informed. To address these issues, direct full-field measurement techniques, like high (angular) resolution electron backscatter diffraction (HR-EBSD) [45, 46] and digital image correlation (DIC) [47, 48], have gained prominence, offering a more accurate and true assessment of the local stresses that drive the failure and deformation mechanisms.

We present a freely available MATLAB-based toolbox to calculate configurational forces and mixed-mode stress intensity factors from displacement and displacement gradient fields. This toolbox enables precise extraction of defect field descriptors, such as the fracture parameters for cracks in isotropic/anisotropic elastic and elastoplastic materials. By utilising only local field data, the toolbox accurately computes mixed-mode SIFs, without the need for predefined specimen geometries or knowledge of the applied loads. Its ability to handle complex geometries and non-standard defect shapes makes it highly adaptable for real-world applications.

2 Theoretical frame and computational implementation

2.1 Numerical evaluation of the *J*-Integral

James Rice [12] formulated a path-independent contour/line integral to capture the configurational forces acting on cracks. Earlier investigations by Sanders [49] and Cherepanov [50] are closely related to Rice's work. Initially, the James-integral or the *J*-integral[1] was defined as the strain energy release rate or work/energy per surface area for cracks subjected to monotonic loading in linear-elastic, plastic-elastic, or plastic materials. This is described in Eq. (4) for an arbitrary contour (Γ) integral around a crack tip, where σ_{ij} and ε_{ij} are the stress and strain tensors, respectively, W is the strain energy density, u_i is the displacement vector components, n_j is the components of the unit vector normal to Γ, ds is the length increment along the Γ and δ is the Kronecker delta, which is 1 if =1 and 0 otherwise.

$$J_k = \int_{\Gamma} \left(W\delta_{kj} - \sigma_{ij}u_{i,k} \right) n_j \, d\Gamma,$$
$$W = \int_0^{\varepsilon_{ij}} \sigma_{ij} \, d\varepsilon_{ij}, \quad k = 1, 2, \tag{4}$$
$$\delta_{kj} = \begin{cases} 1 & if \ k = j \\ 0 & if \ k \neq j \end{cases}$$

Hutchinson [51] and Rice and Rosengren [52] were the first to notice the importance of the *J*-integral as a criterion for crack growth for linear elastic or elastoplastic

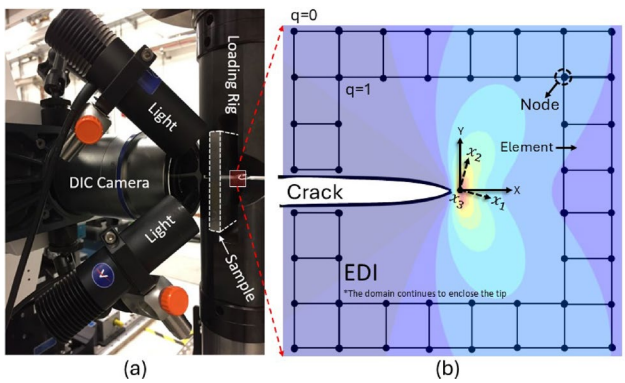

Fig. 1 **a** Experimental setup for in-plane displacement field measurement using digital image correlation on a compact tension specimen with a surface speckle. **b** Representation of the strain field (ε_{22}) overlaid with the crack path and the equivalent domain integration (EDI) scheme. The domain incrementally expands outward from the crack tip, enabling the numerical evaluation of the J_k-integral and mode-decomposed SIFs. Each domain contour corresponds to a discrete area increment (dA) mapped to a regularised measurement grid. The direction of crack extension or virtual crack extension (VCE) vector is assumed along the x_1-axis

[1] In the literature, typically, the *J*-integral is used to mean only the J_1.

(Ramberg-Osgood power hardening) materials. While the original *J*-integral formulation was derived for monotonic loading in nonlinear elastic materials, its application to elastoplastic systems requires careful extension. In particular, the presence of unloading, crack face tractions, and internal residual stresses renders the energy dissipation history-dependent. To address this, various generalisations of the *J*-integral have been proposed, including domain integral formulations, via the finite element method [53–55], that account for plasticity effects and allow for numerical implementation using stress and strain energy fields, including surface traction [56], loading and internal tractions [57], thermal [58, 59] and electrochemical [60], residual stresses [59] and boundary interactions [61–63]. Subsequently, it was expanded to describe cracks in dynamic loading [64], dissimilar materials [65], and also non-crack defects like dislocations [30, 66] and misfitting inclusions [67] as an equivalent descriptor of forces on the defects or their potential energy release rate[2] [68, 69].

While the traditional contour (line) integral relies on an idealised path around the crack tip, domain integration – implemented as the equivalent domain integral (EDI) method [54, 70, 71] – distributes the computation over a larger region, which reduces the sensitivity to both local mesh refinement and numerical errors [70–72], while capturing contributions from plastic dissipation and internal tractions more effectively than a traditional path integral. In this method, an integral along a contour is transformed into an area or volume domain integral containing a weight function that undergoes a smooth linear spatial variation across the domain ($\frac{dq_k}{dx_1}$ in Eq. 5), with magnitude unity inside the domain and zero outside the domain (Fig. 1b) [73]. This enables direct integration of field quantities like stress and strain energy density, making it more robust for nonlinear materials and complex geometries. Additionally, domain integration allows for better handling of plasticity effects, and it improves the numerical stability and accuracy, especially in finite element analysis [74].

EDI is typically coupled with the virtual crack extension (VCE) method that employs Cartesian coordinates aligned with the assumed crack propagation direction. The VCE method then calculates the J_k -integral with the VCE in

[2] While energy release rate and strain energy release rate focus on energy dissipation during crack growth in linear elastic fracture mechanics (LEFM) according to Griffith's theory [49,160]; potential energy release rate refers to the change in potential energy that drives this process. It is equivalent to the energy release rate and strain energy release rate, but framed from a system energy perspective and can be used for both LEFM and non-LEFM. We note that the term 'rate' is often misused in static contexts, as strictly it ought to be reserved for dynamic situations. Using 'flux' instead might be more appropriate in static conditions.

x_k direction. For single defect problems, physically, the two components of the J_k vectors represent unique energy releases induced by the crack movements along the x_1-axis and the x_2-axis [16, 75]. Further details on the significance of the VCE direction are discussed in the first case study in section 4.1.

Thus, a 3D formulation that uses the EDI and VCE will take the following form:

$$J_k = \int_{\mathrm{A}} \left(\sigma_{ij} u_{i,k} - W\delta_{kj}\right) \frac{\partial q_k}{\partial x_j} dA, \quad k = 1,2 \tag{5}$$

where dA is a surface element on a vanishingly small tubular surface enclosing the crack tip.

To simplify the analysis and efficiently compute the J_k -integral without the need to use a shape function to remap element nodes or any other aspects of the finite element method; the VCE direction x_1 is chosen to be parallel to the crack (in practical terms, this can require remapping of experimental data to satisfy this condition so the crack is parallel to the *X*-axis), and the crack tip is located centrally in a square map with an equally spaced grid (typical of experimental measurement) with the measurement points as nodes (Fig. 1b). This simplifies the J_k-integral formulation to:

$$J_k = \sum_{j=1}^{2} \left(\sum_{i=1}^{3} \sigma_{ij} u_{i,\mathrm{k}} - W\delta_{kj} \right) \frac{\partial q}{\partial x_j} dA, \quad k = 1,2 \tag{6}$$

2.2 Numerical evaluation of the *M*-Integral

Budiansky and Rice [16] introduced the *M*-integral as the configurational force of multiple or densely distributed defects in inhomogeneous material, as the assessment of the 'global'[3] or effective damage state [76–78]. For example, it can be used where there is a defect in a material expanding in multiple directions, contrary to the J_k-integral, which evaluates the energy release associated with a singular defect extension. This makes the *M*-integral suitable for multiple and single defects, such as embedded cracks or dislocations pile-up.

As a domain integral, the *M*-integral is formulated as in Eq. 7, which can be simplified when using a regularised mesh to Eq. 8.

$$M_k = \int_{\mathrm{A}} \left(\sigma_{ij}\, u_{i,k}\, x_k - W\, \delta_{kj}\, x_k\right) \frac{\partial q_1}{\partial x_j} dA, \quad k = 1,2 \tag{7}$$

[3] Global covers from having a finite number of defects to the formation of microcracks with random location and orientation.

$$M_k = \sum_{j=1}^{2} \left(\sum_{i=1}^{3} \sigma_{ij} u_{i,\mathrm{k}} x_k - W\delta_{kj} x_j \right) \frac{\partial q_1}{\partial x_j} dA \tag{8}$$

2.3 Numerical evaluation of the stress intensity factors

SIFs are essential in linear elastic fracture mechanics to characterise the magnitude of the crack-tip stress fields, which influence the crack's growth direction and rate [32], but SIFs can also be used with other stress raisers [28, 79]. Since the scalar energy integral cannot distinguish between different loading modes, mode-decoupling techniques are needed to calculate the SIFs, i.e., tensile/compression mode I, in-plane shear mode II, and out-of-plane shear mode III.

We have developed a mode-decoupling technique that introduces an auxiliary displacement gradient ($u_{i,j}$) field to decompose the total displacement gradient field into its symmetric (mode I), in-plane skew-symmetric (mode II), and out-of-plane skew-symmetric (mode III) components. It is achieved by overlaying the auxiliary field onto the total field, mirrored along the VCE vector that is aligned with the x_1-axis, as described in Eq. (6).

$$\begin{aligned}
u_{i,j} &= u^{I}_{i,j} + u^{II}_{i,j} + u^{III}_{i,j} \\
u^{I}_{i,j} &= \frac{1}{2}\begin{pmatrix} u_{1,1}+\bar{u}_{1,1} & u_{1,2}-\bar{u}_{1,2} & u_{1,3}+\bar{u}_{1,3} \\ u_{2,1}-\bar{u}_{2,1} & u_{2,2}+\bar{u}_{2,2} & u_{2,3}-\bar{u}_{2,3} \\ u_{3,1}+\bar{u}_{3,1} & u_{3,2}-\bar{u}_{3,2} & u_{3,3}+\bar{u}_{3,3} \end{pmatrix} \\
u^{II}_{i,j} &= \frac{1}{2}\begin{pmatrix} u_{1,1}-\bar{u}_{1,1} & u_{1,2}+\bar{u}_{1,2} & 0 \\ u_{2,1}+\bar{u}_{2,1} & u_{2,2}-\bar{u}_{2,2} & 0 \\ 0 & 0 & u_{3,3}-\bar{u}_{3,3} \end{pmatrix} \\
u^{III}_{i,j} &= \frac{1}{2}\begin{pmatrix} 0 & 0 & u_{1,3}-\bar{u}_{1,3} \\ 0 & 0 & u_{2,3}+\bar{u}_{2,3} \\ u_{3,1}-\bar{u}_{3,1} & u_{3,2}+\bar{u}_{3,2} & 0 \end{pmatrix}
\end{aligned} \tag{9}$$

For deformation gradient (F) field, the auxiliary field becomes:

$$\begin{aligned}
u_{i,j} &= \sum_{m} F^{m}_{ij} - \delta^{\,m}_{ij}, \quad i,j = 1,2,3, \quad m = I, II, III \\
u^{I}_{i,j} &= \frac{1}{2}\begin{pmatrix} F_{11}+\bar{F}_{11}-2 & F_{12}-\bar{F}_{12} & F_{13}+\bar{F}_{13} \\ F_{21}-\bar{F}_{21} & F_{22}+\bar{F}_{22}-2 & F_{23}-\bar{F}_{23} \\ F_{31}+\bar{F}_{31} & F_{32}-\bar{F}_{32} & F_{33}+\bar{F}_{33}-2 \end{pmatrix} \\
u^{II}_{i,j} &= \frac{1}{2}\begin{pmatrix} F_{11}-\bar{F}_{11} & F_{12}+\bar{F}_{12} & 0 \\ F_{21}+\bar{F}_{21} & F_{22}-\bar{F}_{22} & 0 \\ 0 & 0 & F_{33}-\bar{F}_{33} \end{pmatrix} \\
u^{III}_{i,j} &= \frac{1}{2}\begin{pmatrix} 0 & 0 & F_{13}-\bar{F}_{13} \\ 0 & 0 & F_{23}+\bar{F}_{23} \\ F_{31}-\bar{F}_{31} & F_{32}+\bar{F}_{32} & 0 \end{pmatrix}
\end{aligned} \tag{10}$$

This derivation deviates from previous formulations [70, 72, 80, 81] based on the stress and strain field decomposition, and not the full-field displacement or deformation gradient. Additionally, including $u_{1,3}$, $u_{2,3}$, $u_{3,1}$, $u_{3,2}$ and $u_{3,3}$ in the mode I decomposition and the asymmetrical

part of $u_{3,3}$ in mode II decomposition accounts for out-of-plane displacement gradients associated with the crack opening and in-plane shear, respectively. While classical mode I is defined by normal separation in the crack plane, real-world specimens exhibit non-negligible out-of-plane effects due to Poisson contraction, surface constraints, and front curvature, especially in ductile materials investigated using stereo-DIC. These components capture the symmetric part of the displacement field in the thickness direction and improve accuracy in quantifying opening-mode deformation under mixed loading conditions.

Note that while this decomposition has been validated against analytical mixed-mode solutions (see Sect. 4.1), its sensitivity to non-ideal out-of-plane effects (e.g., Poisson contraction, curvature-induced distortion, or optical artefacts) depends on the quality and nature of the measurement technique. Quantitative assessment of such artefacts is beyond the scope of this study and has been addressed in work involving uncertainty quantification in HR-EBSD [82–84], DIC [85, 86], or DVC [87–89] measurements.

In order to calculate the strain energy density, W; the mode-specific Cauchy's strain tensor (ε) is calculated as in Eq. (10).

$$\varepsilon_{ij}^{m} \approx \frac{1}{2}\left(u_{i,j}^{m} + u_{j,i}^{m}\right), \quad m = I, II, III \tag{11}$$

The mode-specific stress (σ_{ij}^{m}) is calculated from the strains using the material's mechanical properties. Then, from each decomposed field, the mode-specific $J_1^{I+II+III}$ or the *J*-integral can be calculated and related to the specific SIFs, as described in Eq. 12 for the example of an isotropic elastic material with Young's modulus (E), shear modulus (μ) and Poisson's ratio (ν). For anisotropic elastic materials, the eqvalent E, μ and ν can be estimated [90].

$$\begin{aligned} K_I &= \sqrt{E' J_1^I} \\ K_{II} &= \sqrt{E' J_1^{II}} \\ K_{III} &= \sqrt{2\mu J_1^{III}} \\ E' &= \begin{cases} \frac{E}{1-\nu^2} & \text{for plane strain} \\ E & \text{for plane stress} \end{cases}, \\ \mu &= \frac{E}{2(1+\nu)} \end{aligned} \tag{12}$$

$$J_1 = J_1^I + J_1^{II} + J_1^{III}, \quad K_{\text{eff}} = \sqrt{J_1 E'} \tag{13}$$

13)

The effective stress intensity factor K_{eff} is calculated similarly by the summation of the mode-specific $J_1^{I+II+III}$ as in Eq. 13, or from the J_1 calculated directly from the original field; however, some difference between $J_1^{I+II+III}$ and J_1 is expected due to the superimposed auxiliary field for mode decoupling (see Supplementary information: B).

3 Structure of the toolbox

The toolbox, implemented in MATLAB, calculates the configurational forces, namely the *J*-and *M*-integral, and then the mixed-mode SIFS from a displacement or displacement/deformation gradient field. The displacement field is typically measured using 2D in-plane digital image correlation (DIC), 3D-stereo DIC where two cameras measure both in-plane and out-of-plane [91], or 3D digital volume correlation (DVC) [92–94]. The displacement/deformation gradient field can be obtained using micro-diffraction techniques like high-resolution electron backscatter diffraction (HR-EBSD) [95, 96] or differential-aperture X-ray microscopy (DAXM) [97]. The toolbox is organised into several modules that handle user input, data pre-processing, integral and SIF calculations, and post-processing (Fig. 2).

The toolbox requires the user to input the directory of the data, which can be 2D or 3D-stereo displacement data, 2D sliced 3D data, or displacement/deformation gradient data. The user also needs to input the stress state, (typically, plane stress for surface measurement and plane strain for measurement from confined deformation), the measurement length units (meters, millimetres, micrometres, or nanometres), and the material's mechanical properties, which can be an isotropic or anisotropic[4] elastic material, or an elasto-plastic material that follows the Ramberg–Osgood relationship[5] [98].

The input data can be uploaded in any format that MATLAB can read. For 2D displacement measurements, the spatial X and Y coordinates for the displacement U_x in X and displacement U_y in measurement points is needed. 3D-stereo displacement measurements have the additional out-of-plane displacement, with Z spatial coordinates that should equal zero, as such measurements are typically taken at a surface that is effectively flat. For 2D displacement/deformation gradient measurement, along with the measurement points coordinates, the 6 displacement/deformation gradient in-plane components are required. This becomes 9

[4] The user can input the material anisotropic modulus, which can be used to calculate the equivalent Young's modulus, shear modulus and Poisson's ratio for cubic anisotropic materials based on ref. [90]. For non-cubic crystals, the user needs to input the equivalent elastic constants, which can be calculated using different methods, such as the Hashin-Shtrikman method [161] or the Elastic Self-Consistent (ELSC) model [162].

[5] For more details about the Ramberg–Osgood relationship implementation, see the Supplementary information: B.

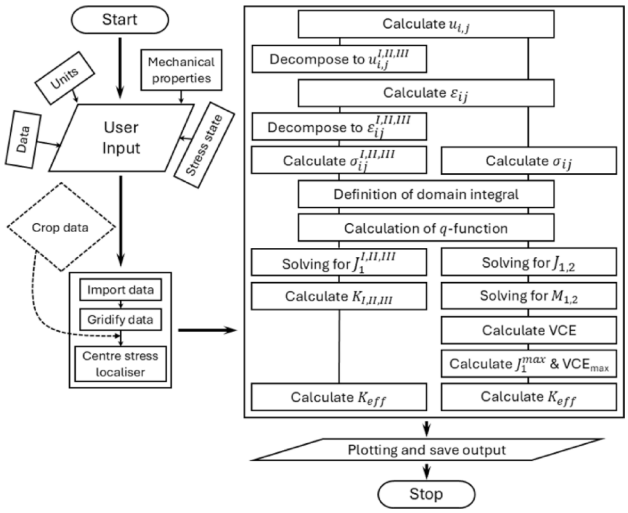

Fig. 2 Workflow of the computational toolbox for extracting configurational forces and stress intensity factors. Flowchart illustrating the key modules of the MATLAB-based toolbox, including data input, preprocessing, invariant integral calculations (*J*- and *M*-integrals), mode decomposition, and post-processing. Solid arrows represent the core computational pipeline, while dashed lines indicate optional or user-controlled functionalities. The workflow accommodates both 2D and 3D displacement, or displacement/deformation gradient data and supports materials with isotropic, anisotropic, or elastoplastic behaviour

components for 3D-stereo displacement/deformation gradient measurement.

Poor quality or uncertain data may arise for various reasons, including material discontinuities [99, 100] like grain boundaries or crack faces. These must be removed from the data and replaced with NaNs (not a number). The input deformation field must also be restricted to one defect or agglomeration of defects that do not strongly interact with other defects (including grain boundaries), as that will affect the path independence of the invariant integrals [101–103].

The toolbox requires the data to be a regularised mesh or measurement points with a constant step size, which is commonplace for most experimental methods. A comparably coarse step size is sufficient for invariant-integral calculations, with no refinement near the defect being needed [104]. However, if this is not the case, once the data is uploaded, it will be automatically mapped into equally spaced grids, i.e., a square grid with four nodes/data points.

Following the data reading, the user locates the defect. For a crack, that will be the crack tip, and for a dislocation, that will be its core. The user then defines a square around the defect that will be used to calculate the invariant integrals through the equivalent domain integral (EDI) method. The displacement gradient is then calculated and decoupled into $u_{i,j}^{I}$, $u_{i,j}^{II}$, $u_{i,j}^{III}$ for mode I–III. The strain is calculated from the decomposed displacement or deformation gradient, as explained in section 2.3. Then, the stress is calculated depending on the material's stress-strain relationship.

As explained above, the *J*- and *M*-integrals are calculated using the equivalent domain integral (EDI) method coupled with the virtual crack extension (VCE) [73, 105] parallel to the horizon or X-axis, i.e., $\theta = 0°$ (illustrated in Fig. 1). To explore changes in the VCE direction (or θ), the field can be transformed using a rotation matrix (R_θ) as follows:

$$u_{i,j}^{\theta} = R_{z(\theta)}\, u_{i,j}\, R_{z(\theta)}^{T}$$
$$R_{z(\theta)} = \begin{bmatrix} \cos(\theta) & -\sin(\theta) & 0 \\ \sin(\theta) & \cos(\theta) & 0 \\ 0 & 0 & 1 \end{bmatrix} \tag{14}$$

While the toolbox requires specifying a defect location and VCE direction, these parameters can be derived directly from the displacement field. For example, crack tips can be identified through field gradient analysis or phase congruency filters [106–109], and the VCE direction can be iteratively refined by comparing J_1 and J_2 values across directions. This removes the need for predefined geometry or load assumptions and allows the analysis to adapt to arbitrary crack shapes and propagation paths.

Next, the user selects the number of expanded domains to consider by inspecting the *J*-integral's convergence, since convergence may fail when the integration domain extends into peripheral stress fields. As discussed in prior research [101–103], contributions from surrounding gradient fields can disrupt path independence unless fully enclosed within the integration domain. The mean and standard deviation of the invariant integrals and SIFs are calculated where stable convergence has been achieved (shaded pink in Fig. 3b).

4 Illustrative examples

To demonstrate the versatility of the toolbox, below we present several case studies where we used a (1) 3D-stereo synthetic displacement field for a mixed mode crack to validate the toolbox, (2) high-resolution electron backscatter diffraction (HR-EBSD) displacement gradient field around a micro-crack in a single crystal ceramic, (3) high-resolution transmission Kikuchi diffraction (HR-TKD) displacement gradient field mapped around a dislocation in an anisotropic metal, and (4) 3D displacement field obtained by digital volume correlation (DVC) of computed X-ray tomographs of a fatigue crack with complicated geometry.

4.1 Case study 1: analytical field benchmarking

A mixed-mode crack displacement field that has a mode I stress intensity factor (K_I) of 3 MPa m$^{0.5}$, mode II (K_{II}) of 1 MPa m$^{0.5}$, and mode III (K_{III}) of 2 MPa m$^{0.5}$ was created using the Westergaard analytical solution [110], with the assumption of plane stress conditions (Eq. 12 to 15). The material mechanical properties were defined as linear isotropic with Young's modulus (E) of 210 GPa and Poisson's ratio (υ) of 0.3. The field of view was 200 × 200 mm^2, comprised of 4 × 4 mm^2 square elements with the crack tip at the centre.

$$u_x = \frac{K_I}{2\mu}\sqrt{\frac{r}{2\pi}}\cos\left(\frac{\theta}{2}\right)\left[k-1+2\sin^2\left(\frac{\theta}{2}\right)\right] + \frac{K_{II}}{2\mu}\sqrt{\frac{r}{2\pi}}\sin\left(\frac{\theta}{2}\right)\left[k+1+2\cos^2\left(\frac{\theta}{2}\right)\right] \tag{15}$$

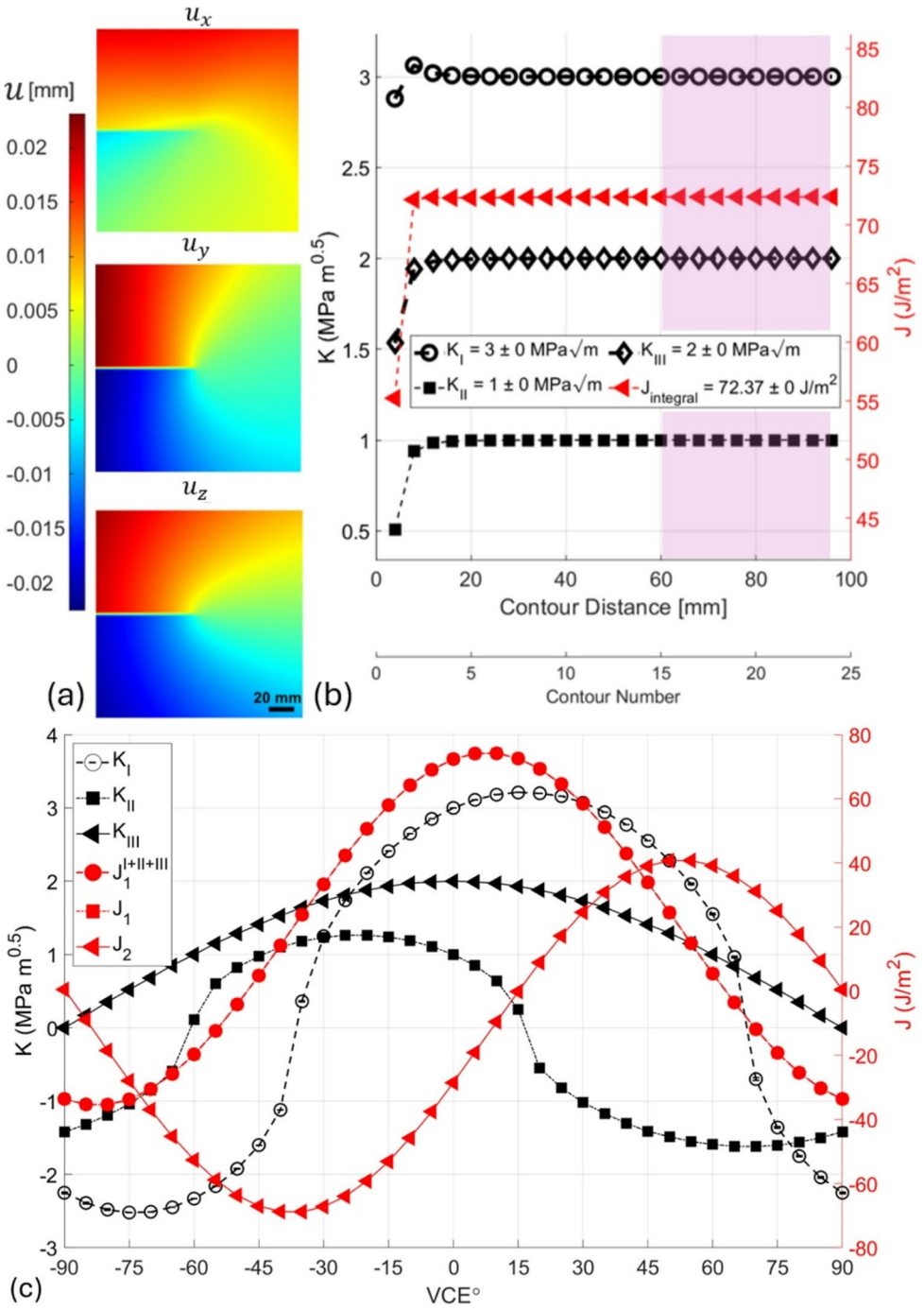

Fig. 3 Validation of the toolbox using synthetic displacement fields for a stationary mixed-mode crack: **a** Synthetic displacement field generated using Westergaard's solution for a stationary crack under mixed-mode loading: (mode I: 3 MPa m$^{0.5}$, mode II: 1 MPa m$^{0.5}$, and mode III: 2 MPa m$^{0.5}$), assuming plane stress conditions. The field of view spans 200 × 200 mm² with a crack tip at the centre. **b** Calculated *J*-integral and decomposed SIFs for modes I–III as a function of domain expansion using the EDI method. Convergence trends are shown as the domain extends away from the crack tip, demonstrating accurate recovery of input values. **c** The sensitivity of the J_k-integral and SIF components to the direction of the VCE, varied from −90° to +90° in 5° increments. J_1 directly calculated from the field, and $J_1^{I+I+III}$ calculated from summing the mode-specific J_1 overlap

$$u_y = \frac{K_I}{2\mu}\sqrt{\frac{r}{2\pi}}\cos\left(\frac{\theta}{2}\right)\left[k+1-2\cos^2\left(\frac{\theta}{2}\right)\right] - \frac{K_{II}}{2\mu}\sqrt{\frac{r}{2\pi}}\cos\left(\frac{\theta}{2}\right)\left[k-1-2\sin^2\left(\frac{\theta}{2}\right)\right] \quad (16)$$

$$u_z = \frac{2K_{III}}{\mu}\sqrt{\frac{r}{2\pi}}\sin\left(\frac{\theta}{2}\right) \quad (17)$$

$$k = \frac{3-v}{1+v} \quad (18)$$

The mixed-mode SIFs computed by the toolbox from this synthetic displacement field matched with the prescribed inputs mode I–III (Fig. 3b). The presence of highly localised fields near the crack tip detrimentally influences the initial convergence of the integral; however, convergence stabilises as the integration domain expands, which is expected due to the crack-tip singularity [110]. At very small radii, numerical noise and steep gradients affect stability. As the domain expands to enclose the energy release zone, the configurational force estimate stabilises. While no universal criterion applies, in practice, the measured displacement or gradient field must span a sufficiently broad region around the crack or defect to allow such convergence, and the region immediately adjacent to the singularity should be excluded from the integration contour.

Additional factors affecting convergence, such as noise and uncertainty in the crack position, are examined further in the Supplementary information: A. In addition to the analytical benchmark, we validated the decomposition against a finite element displacement field generated in Abaqus. The recovered SIFs closely matched the known applied values, further supporting the generalisability of the approach beyond idealised cases (see Supplementary Information: B).

The VCE direction was then varied from − 90° to 90° with a step size of 5°, by transforming the input field, to study the effect of the assumed VCE direction on the calculations. As shown in Fig. 3c, the energy release and mechanical conditions at the crack tip change with direction because if the crack propagates in the assumed VCE direction, the magnitudes of the modes of the mechanical conditions differ at the tip. This variation associated with the VCE might be used in fracture experiments to test criteria that describe mixed-mode crack propagation, which is still a point of contention [111–114].

Energy-based criteria that use the energy-based path integrals or strain energy density appear to hold great potential for both elastic and elastoplastic materials [112–115], especially for dynamic loading [116]. For the current synthetic data, and using the Newton-Raphson method for a solution that maximises J_1, we found that θ_{max} is at 7.44°, which results in a J_1 of 74.33 J m^{-2} and J_2 of -14.47 J m^{-2}, with the SIFs for this direction being 3.15 MPa m$^{0.5}$ for mode I, 0.76 MPa m$^{0.5}$ for mode II, and 1.98 MPa m$^{0.5}$ for mode III. Thus, under these conditions, the crack is expected to slightly deflect (or kink) to maximise its energy [117, 118].

Given the strong sinusoidal relationship between the J_1, J_2 and the VCE, the outputs can be fitted by Eq. 16, without considering the offset via a rotation matrix, but we encourage the reader to consider formulating a more elegant solution that considers the offset.

$$J_k^\theta = R_{k,\theta}\, J_k, \quad k = 1,2$$
$$R_\theta = \begin{bmatrix} cos\theta & -sin\theta \\ sin\theta & cos\theta \end{bmatrix} \quad (19)$$

4.2 Case study 2: Mixed-mode micro-crack in a brittle ceramic (6 H-SiC)

Measuring microscale fracture toughness is vital for assessing the durability of brittle coatings and hard surfaces under stress. Microscale fracture toughness, particularly for brittle coatings and hard surfaces, is often estimated using indentation-induced cracking and empirical equations based on assumptions about crack geometry and loading conditions. Here, we used data from Leide et al. [119] where a stress-free (0001) 6 H-SiC single crystal was nano-indented with a Berkovich tip (Fig. 4a), employing the continuous stiffness method (CSM) with 2 nm harmonic displacement at 45 Hz, and a 0.05 s^{-1} strain rate. EBSD was performed on a Zeiss Merlin FEG-SEM using a Bruker detector, capturing high-resolution diffraction patterns at 100 nm steps and 50 ms per pixel at the 1-µm-deep indent. Via the CrossCourt software, patterns were processed using FFT-based cross-correlation (i.e., HR-EBSD) across 40 overlapping regions of interest to compute the elastic displacement gradient tensors.

The elastic displacement gradient field at one of the cracks (dashed box in Fig. 4b) caused by the indent was analysed with the toolbox to assess the conditions at the crack tip. The crack is parallel to $\left[1\ \bar{1}\ 00\right]$, which is the trace of the expected $\left(11\ \bar{2}\ 0\right)$ cleavage plane. The VCE direction was assumed parallel to the crack, with the integration domain expanding at 100 nm per domain from the crack tip. Stable convergence, pink shaded area in Fig. 4c, was achieved 1.2 µm ahead of the crack tip, revealing a mixed

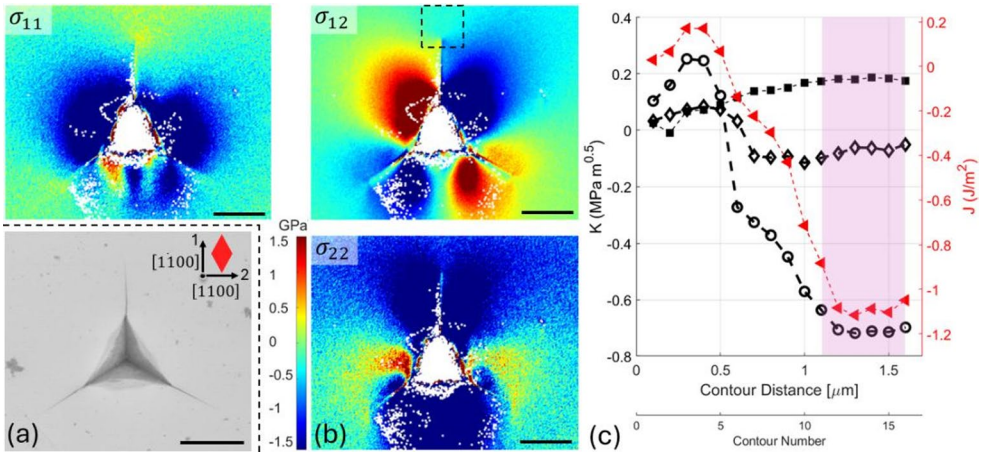

Fig. 4 **a** SEM image of the nano-indented (0001) 6 H-SiC single crystal with the axes and the crystal orientation. **b** The in-plane stress components calculated from HR-EBSD using anisotropic Hooke's law and the (0001) 6H-SiC material anisotropic stiffness matrix, with ε_{33} strain calculated with plane stress assumption. **c**) *J*-integral and SIFs convergence for the crack dashed in b. The scale bar is 5 µm

mode crack field with mode I of -0.70±0.03 MPa m$^{0.5}$, mode II of 0.18±0.17 MPa m$^{0.5}$, mode III of -0.07±0.02, and *J*-integral of -1.05±0.08 J m^{-2}. The signs of mode II (in-plane shear) and mode III (out-of-plane shear) components depend on the nodal configuration and symmetry in the field and do not reflect physically meaningful directionality. In contrast, the sign of mode I (tensile vs. compressive) is physically significant.

Cracking during sharp indentation of hard materials arises from the highly localised stress fields generated beneath the indenter. The geometry of the Berkovich tip produces significant triaxial tensile stresses at and around the contact zone during indentation [120], which can exceed the material's fracture toughness [121, 122]. In 6H-SiC, which exhibits limited plasticity and is brittle, these stresses initiate radial cracks along the weak cleavage planes, i.e., the $\left\{11\ \bar{2}\ 0\right\}$ prismatic planes in the orientation of this experiment. Upon unloading, the interaction between the indentation-induced plastic zone and the surrounding elastic matrix leads to a residual stress field. Spallation may occur when the residual stresses are sufficiently high to cause lateral fractures on shallow subsurface cleavage planes (e.g. the basal plane in the orientation of this experiment).

Here, no spallation was observed, and the stress map (Fig. 4b), which was measured after unloading, shows the elastic recovery generated compressive residual stresses. The negative *J*-integral and mode I SIF both show that the radial crack is effectively clamped shut after unloading. The mode II and III SIFs show that the residual stress also causes a small, but measurable, shear loading of the crack. Although the indentation-induced crack is not in critical condition, the toolbox can be used to evaluate the fracture toughness by measuring the mixed-mode crack tip field of a static crack at the critical condition for crack propagation, as done in [123] for cleavage in single-crystal silicon.

4.3 Case study 3: edge dislocation in anisotropic tungsten

Dislocations are one of the most important defects in solids, since they influence the properties of crystals, not only the mechanical, but also the electric, magnetic, optic, and semi-conducting properties [124–126] as well as the growth of crystals [127]. Here, we use the data collected by Yu et al. [128], where they employed high-resolution transmission Kikuchi diffraction (HR-TKD) to map the full elastic displacement gradient induced by a single edge dislocation in pure tungsten (Fig. 5a). Yu et al. then compared the measured field to forward calculations based on an elastically isotropic dislocation model and its Burgers vector [129], demonstrating a high degree of agreement and validating the capability of HR-TKD for resolving lattice distortions at the nanoscale.

The input to the toolbox was the full 3D displacement gradient tensor obtained from HR-TKD, including all nine components, mapped onto a regularised measurement grid. We then transformed the measured displacement gradient field so that the VCE had the same direction as the $\left[1\ \bar{1}\ 1\right]a/2$ Burgers vector. The anisotropic stiffness matrix for pure body-centred cubic tungsten ($C_{11} = 522.39,\ C_{44} = 160.83,\ C_{12} = 204.37$ in GPa) was transformed to the frame of reference using a rotation matrix (R_{ϕ_1,Φ,ϕ_2}) constructed from the Euler angles (ϕ_1, Φ, ϕ_2) of the reference pattern (measured remote from the defect) as in Eq. (17) [130].

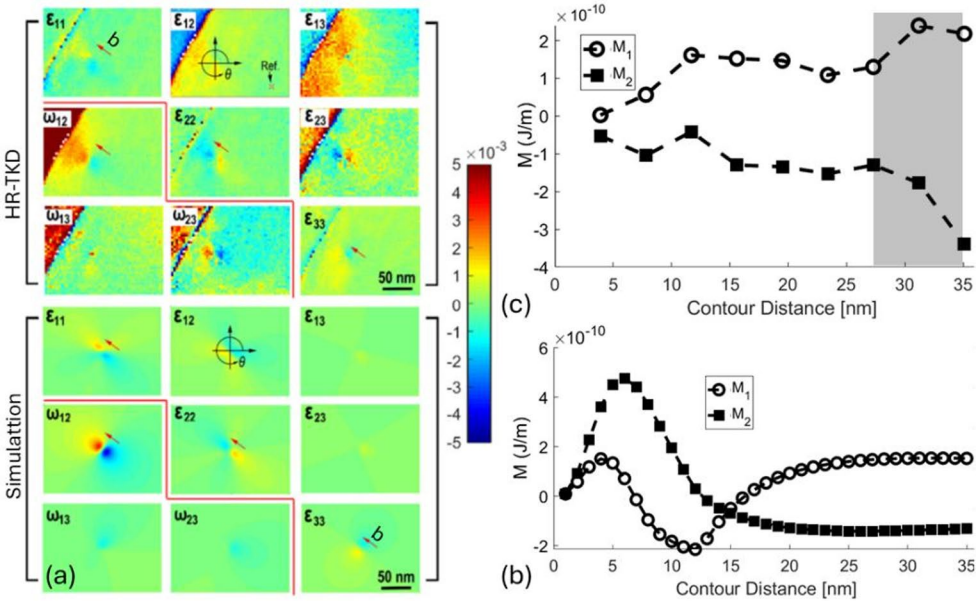

Fig. 5 Application of the toolbox to experimental and simulated dislocation fields in anisotropic tungsten. **a** High-resolution transmission Kikuchi diffraction (HR-TKD) and simulated maps of the three-dimensional lattice strain tensor and lattice rotations around an edge dislocation in pure tungsten (reproduced from [128]). **b***M*-integral convergence for the **b** simulated and **c** experimental dislocation fields, with shaded area, denotes the loss of convergence in the HR-TKD field beyond 15.6 nm due to interference from the grain boundary (top left in a) and measurement distortions near boundaries

$$R_{\phi_1,\Phi,\phi_2} = \begin{bmatrix} \cos\phi_1\cos\phi_2 - \cos\Phi\sin\phi_1\sin\phi_2 & \cos\Phi\cos\phi_1\sin\phi_2 + \sin\phi_1\cos\phi_2 & \sin\Phi\sin\phi_2 \\ -\cos\phi_1\sin\phi_2 - \cos\Phi\sin\phi_1\cos\phi_2 & \cos\Phi\cos\phi_1\cos\phi_2 - \sin\phi_1\sin\phi_2 & \sin\Phi\cos\phi_2 \\ \sin\Phi\sin\phi_1 & -\sin\Phi\cos\phi_1 & \cos\Phi \end{bmatrix} \tag{20}$$

By using the rotation matrix, the anisotropic elastic stiffness matrix, C_{ijkl}, can be mapped from the reference crystal coordinate system to the local coordinate system as below [127, 131]:

$$C^*_{ijkl} = T_\sigma^{-1}\, C_{ijkl}\, T_\varepsilon \tag{21}$$

where the stress and strain transformation tensor, T_σ and T_ϵ, account for how stresses and strain change under coordinate rotation, respectively, and they are calculated from the rotation matrix as follows:

The toolbox used the experimental and simulated dislocation displacement gradient fields to calculate the dislocation's configurational force, i.e., the *M*-integral. For the high-resolution simulated data, the domain integration started from the dislocation core and expanded gradually with an increment of 1 nm (Fig. 5b). Convergence was achieved once the domain expanded to engulf the dislocation at around 20 nm, with results of $M_1 = 0.142 \pm 0.014$ nJ m^{-1} and $M_2 = -0.138 \pm 0.003$ nJ m^{-1}.

$$T_\sigma = \begin{bmatrix} R_{11}^2 & R_{12}^2 & R_{13}^2 & 2R_{12}R_{13} & 2R_{11}R_{13} & 2R_{11}R_{12} \\ R_{21}^2 & R_{22}^2 & R_{23}^2 & 2R_{22}R_{23} & 2R_{21}R_{23} & 2R_{21}R_{22} \\ R_{31}^2 & R_{32}^2 & R_{33}^2 & 2R_{32}R_{33} & 2R_{31}R_{33} & 2R_{31}R_{32} \\ R_{21}R_{31} & R_{22}R_{32} & R_{23}R_{33} & R_{22}R_{33}+R_{23}R_{32} & R_{21}R_{33}+R_{23}R_{31} & R_{21}R_{32}+R_{22}R_{31} \\ R_{11}R_{31} & R_{12}R_{32} & R_{13}R_{33} & R_{12}R_{33}+R_{13}R_{32} & R_{11}R_{33}+R_{13}R_{31} & R_{11}R_{32}+R_{12}R_{31} \\ R_{11}R_{21} & R_{12}R_{22} & R_{13}R_{23} & R_{12}R_{23}+R_{13}R_{22} & R_{11}R_{23}+R_{13}R_{21} & R_{11}R_{22}+R_{12}R_{21} \end{bmatrix} \tag{22}$$

$$T_\varepsilon = \begin{bmatrix} R_{11}^2 & R_{12}^2 & R_{13}^2 & R_{12}R_{13} & R_{11}R_{13} & R_{11}R_{12} \\ R_{21}^2 & R_{22}^2 & R_{23}^2 & R_{22}R_{23} & R_{21}R_{23} & R_{21}R_{22} \\ R_{31}^2 & R_{32}^2 & R_{33}^2 & R_{32}R_{33} & R_{31}R_{33} & R_{31}R_{32} \\ 2R_{21}R_{31} & 2R_{22}R_{32} & 2R_{23}R_{33} & R_{22}R_{33}+R_{23}R_{32} & R_{21}R_{33}+R_{23}R_{31} & R_{21}R_{32}+R_{22}R_{31} \\ 2R_{11}R_{31} & 2R_{12}R_{32} & 2R_{13}R_{33} & R_{12}R_{33}+R_{13}R_{32} & R_{11}R_{33}+R_{13}R_{31} & R_{11}R_{32}+R_{12}R_{31} \\ 2R_{11}R_{21} & 2R_{12}R_{22} & 2R_{13}R_{23} & R_{13}R_{23}+R_{13}R_{22} & R_{11}R_{23}+R_{13}R_{21} & R_{11}R_{22}+R_{12}R_{21} \end{bmatrix} \tag{23}$$

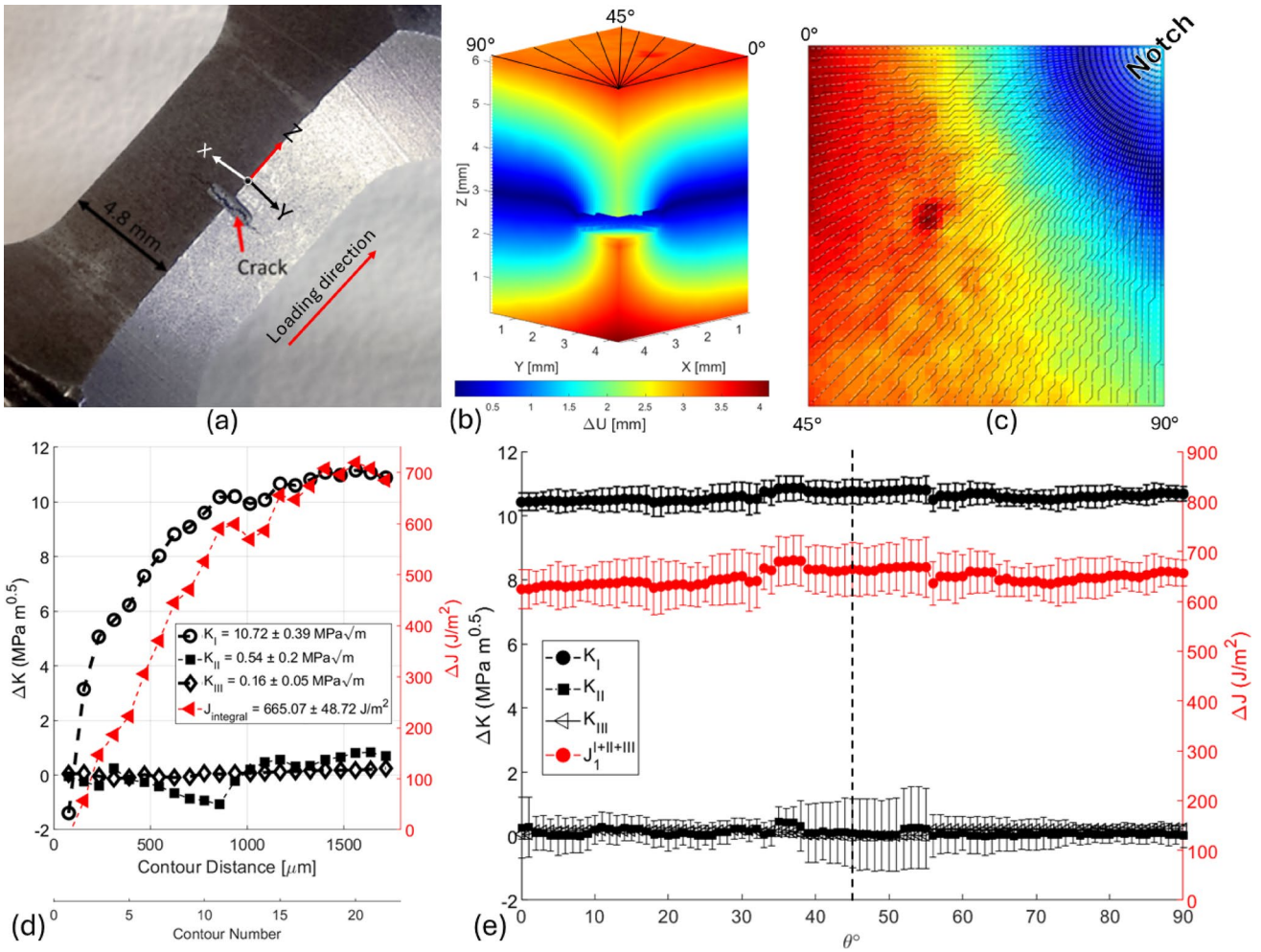

Fig. 6 Analysis of a 3D displacement field from a fatigue crack using the computational toolbox. **a** Optical image of a compact tension specimen showing the notch and a fully developed fatigue crack. **b** The three-dimensional displacement field (U_z), aligned with the loading direction, was measured via DVC after 230,000 loading cycles (P_{min} = 450 N, P_{max} = 4500 N). Displacement field extracted with a 96 × 96 × 96 voxel subset and 75% overlap. **c** Illustration of the radial slicing of the crack front used for virtual crack extension (VCE) analysis, with layers sampled from 0° to 90° along the crack edge at 1° intervals. **d** $J_1^{I,III,III}$ integral and SIFs convergence for the crack front at 33°, showing stable convergence, using the equivalent domain integral method, 1 mm away from the crack tip. **e** Mode I–III and the *J*-integral across the crack front, revealing dominant mode I

As for the relatively low-resolution experimental data, the domain integration expanded in increments of 3.9 nm, and convergence was achieved at 15.6 nm from the core (Fig. 5c). However, once the domain reached the grain boundary (shaded area in Fig. 5c), it lost convergence as the grain boundary also acts as a stress localiser. More importantly, the displacement gradient field calculated from the Kikuchi patterns near the grain boundaries is unreliable due to the beam volume interaction with both grains near the grain boundary, which causes pattern distortion [132]. The analysis of the experimental observation of the dislocation found $M_1 = 0.134 \pm 0.020$ nJ m^{-1} and $M_2 = -0.137 \pm 0.011$ nJ m^{-1}, which agrees with the simulation.

4.4 Case study 4: 3D displacement field of a fatigue crack

Fatigue crack growth under cyclic loading is a critical failure mechanism in structural materials, and understanding the local mechanical conditions around the crack front is essential for predicting durability and lifetime [92–94]. Here, we used an in-situ synchrotron X-ray computed tomography (XCT) dataset from observations of a fatigue crack in nodular cast iron. The data considered here were collected for a well-developed crack at two different loads, after 230,000 loading cycles of P_{min} = 450 N and P_{max} = 4500 N [133]. The three-dimensional displacement field was determined from the image volumes by local DVC using a subset of 96 × 96 × 96 voxels with 75% overlap, yielding high-resolution

measurements of the U_x, U_y, and U_z components. Figure 6a shows the specimen and the notch–crack geometry.

Before using the toolbox, phase congruency filtering of the displacement field was used to isolate the crack region and remove noisy data along the crack faces (Fig. 6b), as DVC struggles near crack faces due to edge effects [99, 100]. Additionally, a reference point was identified and set as the origin to correct for rigid body motions and ensure accurate field interpretation [134]. This ensured that all measured displacements accurately reflected the material's deformation, free from artefacts caused by sample movement during testing. To examine the radial nature of the field around the curved crack front, the displacement field was sectioned without extrapolation into angular layers from 0° to 90° (Fig. 6c). Each section was analysed as a 2D problem, using the EDI method, aligned with the local crack front direction using linear elastic material properties of $E = 158$ GPa and $\nu = 0.3$ [135] and assuming plane strain conditions, as the XCT measurement started 0.3 mm deep in the sample.

Figure 6d shows an example of the convergence of the *J*-integral in the 33° section, where stable integration was achieved after a contour size of 1 mm. The resulting SIFs at 33° indicate a dominant mode I of 10.72 ± 0.39 MPa $m^{0.5}$, with insignificant mode II of 0.54 ± 0.20 MPa $m^{0.5}$ and mode III of 0.16 ± 0.05 MPa $m^{0.5}$. Overall, the variation around the curved crack front (Fig. 6e) shows that the mechanical loading was predominantly mode I at 10.61 ± 0.12 MPa $m^{0.5}$. The average mode I SIF is consistent with the original publication and the observed crack growth rate [133, 136]. The distribution of mode I SIFs along the crack front differs slightly from that reported in the original publication [133], in which the calculated mode I values were distributed more asymmetrically. That analysis, in which it was assumed that the mode III could be neglected, was performed using a finite element-based method in Abaqus. In contrast, the present results were obtained directly from the experimental DVC field using the path-independent integrals implemented in the toolbox to consider all modes. Differences in the assumed crack propagation direction could also affect the analysis, influencing the mode decomposition.

It is important to note that the method worked on this experimental data because the load is predominantly in the opening direction. However, where there is a significant out-of-plane displacement component, direct application of the decomposition method does not allow for stress equilibrium in the far-field of the crack for the case of mode III, which affects the convergence of the J_1^{III}-integral and leads to overestimation of mode III [137], as shown in the Supplementary information: C. This is not a limitation of the toolbox itself but reflects the difficulty of resolving equilibrium-consistent mode III fields from DVC data. Users should therefore interpret Mode III values cautiously unless validated through simulation or corrected using inverse modelling techniques. Future work may address this by integrating equilibrium-enforcing corrections [138].

5 Discussion

The presented computational toolbox offers a generalisable and robust method for extracting fracture parameters (i.e. configurational forces and mixed-mode stress intensity factors) directly from experimental displacement and gradient fields, without requiring predefined geometry, boundary conditions, or numerical meshing. Its validity and versatility are demonstrated across synthetic, 2D experimental, and 3D datasets, including microcracks in a ceramic, dislocations in anisotropic materials and fatigue cracks in cast iron. The method reliably handles complex defect morphologies and noisy[6] displacement fields, and it is well-suited for experimental platforms such as DIC, DVC, HR-EBSD and HR-TKD. The accuracy of the extracted stress intensity factors and configurational forces depends directly on the quality of the input field data. The toolbox does not compensate for measurement artefacts, equilibrium violations, or poor resolution; rather, it is designed to extract physical quantities from well-resolved, experimentally consistent displacement or deformation gradient fields. Users should ensure appropriate filtering, denoising, or validation when working with experimental data. Simply put, the method performs well when fed good data; poor-quality input will yield unreliable outputs.

Microscale fracture toughness, particularly for brittle coatings and hard surfaces, is often estimated using indentation-induced cracking and empirical equations based on assumptions about crack geometry [121, 122, 139] and loading conditions [140]. A widely used approach, developed by Lawn et al. [40, 141–143], relates mode I fracture toughness to measurable parameters from Vickers indentation, though variations like Berkovich indentation exist [144]. However, the method suffers from uncertainties [145], such as ambiguous subsurface crack shapes [143], variability in fitting factors [146], and material-specific deformation behaviours, like phase transformations in silicon [147, 148]. These complexities, along with user bias and material anisotropy [149–151], raise concerns about the accuracy and reliability of indentation-based toughness values, leading some to argue that such data should be used only comparatively [152].

The presented computational toolbox is a potential game changer, enabling more rigorous, geometry-independent, and physically meaningful evaluation of fracture toughness

[6] Within limits outlined in the Supplementary Information: A.

at the microscale, overcoming the limitations of empirical indentation models by directly quantifying stress intensity factors and energy release rates from experimentally measured fields. Although the toolbox is general in formulation, the present implementation is grounded in small-strain theory, limiting its immediate applicability to materials such as metals and ceramics where these assumptions hold. Extending the framework to support finite-deformation mechanics would enable its application to soft hyperelastic materials. Recent work [153] offers a promising foundation for incorporating configurational force formulations under large strain, and integrating such capabilities is a key direction for future development.

Nonetheless, for path-independent energy integrals to yield meaningful results, the integration domain must fully enclose the region influenced by the defect. The integral may become path-dependent if the domain fails to capture the localised strain fields. This can occur, for example, near a plastically strained crack tip, as in the presence of significant plastic deformation, the energy integrals may exhibit path dependence until the integration domain fully encompasses the plastic zone [102]. Also, pronounced deformation of microstructurally heterogeneous materials might be an issue, particularly in small-scale experiments or when the defect field interacts with boundaries or neighbouring defects. These factors need to be considered when designing experiments, i.e., microstructure length-scale, field of view and spatial resolution of measurements. Once these are considered, the computational framework presented here provides a robust and generalisable solution, particularly for analysing complex and non-standard defect geometries. Its ability to handle anisotropic and elastoplastic materials[7], as well as 3D displacement fields, enables the investigation of real-world microstructural damage scenarios.

In addition, incorporating DIC, DVC, and diffraction-based techniques (e.g., HR-TKD, HR-EBSD) bridges the gap between experimental measurements and computational mechanics. By directly processing experimentally acquired local field data, the toolbox eliminates the need for global load measurements or assumptions about boundary conditions. This significantly reduces uncertainties caused by misalignment, residual stresses, or compliance effects commonly affecting conventional approaches [154, 155].

While the toolbox is primarily designed to operate on full deformation or displacement gradient fields, it can also be applied to strain measurements, such as those obtained using X-ray [156] or neutron diffraction [157]. However, as these methods provide only the symmetric strain tensor, they do not capture the full deformation gradient, which includes antisymmetric components related to lattice rotations. To approximate the off-diagonal components, numerical integration techniques could be employed to approximate these components [158], provided that sufficient spatial resolution and boundary conditions are available.

Overall, the toolbox addresses a long-standing challenge in materials characterisation, linking high-resolution experimental measurements to actionable mechanical descriptors. It is particularly suited for applications in fatigue crack growth studies, microstructure-sensitive failure analysis, and defect quantification in advanced manufacturing processes. In addition, the toolbox aligns with the vision of Material Testing 2.0 [159], emphasising the shift from conventional, idealised mechanical testing to automated, high-throughput, data-driven characterisation. The computerised processing pipeline allows for the efficient analysis of large datasets from advanced imaging techniques such as synchrotron X-ray tomography and high-resolution electron microscopy, thus supporting accelerated materials qualification and predictive maintenance workflows.

6 Conclusions

We have formulated, implemented, and validated a general-purpose computational toolbox for extracting configurational forces and mixed-mode stress intensity factors from experimentally measured displacement or deformation gradient fields. The method implements path-independent energy integrals, including the J- and M-integrals, and introduces a novel mode decomposition approach that does not rely on predefined boundary conditions or external loads. Validation across synthetic and experimental datasets, including HR-EBSD, HR-TKD, and 3D-stereo DIC, demonstrates the toolbox's robustness, accuracy, and versatility in 2D and 3D across different length-scales. The toolbox bridges a critical gap between experimental and theoretical mechanics frameworks by enabling quantitative, geometry-independent defect analysis.

Supplementary Information The online version contains supplementary material available at https://doi.org/10.1007/s00366-025-02262-5.

Acknowledgements The authors thank Dr Hongbing Yu (Canadian Nuclear Laboratories) for sharing the dislocation deformation field data, and Dr Alexander Leide (UK Atomic Energy Authority) for sharing the 6 H-SiC EBSD data. The authors are grateful for the financial support provided by the Engineering and Physical Sciences Research Council (EPSRC) (Grant ref EP/N509711/1), the University of Cape Town, and the Sudanese Materials Scientists and Engineers (SMSE).

Author contributions AK: Conceptualisation, Methodology, Software, Visualisation, Investigation, Formal analysis, Writing - original draft. AA: Investigation, Formal analysis, Writing - original draft. TB: Methodology, Writing - review & editing. TJM: Resources, Writing -

[7] See Supplementary information: B for a case study on an elastoplastic material.

review & editing.

Data availability The data that support the findings of this study are available at https://github.com/Shi2oon/Defect_Descriptor.

Code availability The MATLAB-based toolbox developed in this study is openly available under an MIT license. A permanently archived version of the code, including example datasets and documentation, is accessible via Zenodo at https://doi.org/10.5281/zenodo.6411484, ensuring compliance with the FAIR (Findable, Accessible, Interoperable, and Reusable) principles. A continuously maintained and updated toolbox version is hosted on GitHub at https://github.com/Shi2oon/Defect_Descriptor.

Declarations

Conflict of interest The authors declare no competing interests.

References

1. Asaro R, Lubarda V (2006) Basic integral Theorems. Mechanics of solids and materials. Cambridge University Press, Cambridge, pp 26–35. https://doi.org/10.1017/CBO9780511755514.003
2. Noether E Invariante Variationsprobleme. Nachrichten von der gesellschaft der wissenschaften Zu Göttingen. Mathematisch-Physikalische Klasse 1918:235–257
3. Noether E (1971) Invariant variation problems. Transp Theory Stat Phys 1:186–207. https://doi.org/10.1080/00411457108231446
4. Asaro R, Lubarda V (2006) Forces and energy in elastic Systems. Mechanics of solids and materials. Cambridge University Press, Cambridge, pp 355–374. https://doi.org/10.1017/CBO9780511755514.022
5. Günther W (1962) Über einige randintegrale der elastomechanik. Abh Brauchschw Wiss Ges 14:53–72
6. Eshelby JD (1975) The elastic energy-momentum tensor. J Elast 5:321–335. https://doi.org/10.1007/BF00126994
7. Atkinson C, Eshelby JD (1968) The flow of energy into the tip of a moving crack. Int J FractMech 4:3–8. https://doi.org/10.1007/BF00189137
8. Lubarda VA (2019) Dislocation burgers vector and the Peach–Koehler force: a review. J Mater Res Technol 8:1550–1565. https://doi.org/10.1016/j.jmrt.2018.08.014
9. Kirchner H (1999) The force on an elastic singularity in a non-homogeneous medium. J Mech Phys Solids 47:993–998. https://doi.org/10.1016/S0022-5096(98)00070-2
10. Paidar V, Lejček L (eds) (1984) Kirchner. Dislocation fields. The structure and properties of crystal defects. Elsevier, pp 370–383
11. Peter M, Anderson JP, Hirth (2017) Jens Lothe. Theory of dislocations, 3rd edn. Cambridge University Press, Cambridge
12. Rice JR (1968) A path independent integral and the approximate analysis of strain concentration by notches and cracks. J Appl Mech 35:379–386. https://doi.org/10.1115/1.3601206
13. Asaro R, Lubarda V (2006) Dislocations and cracks: elementary Treatment. Mechanics of solids and materials. Cambridge University Press, Cambridge, pp 293–298. https://doi.org/10.1017/CBO9780511755514.018
14. Maugin GA (2016) Configurational Forces. Boca raton. Chapman and Hall/CRC, Florida. https://doi.org/10.1201/b10356
15. Sih GC, Paris PC, Erdogan F, Crack-Tip (1962) Stress-Intensity factors for plane extension and plate bending problems. J Appl Mech 29:306–312. https://doi.org/10.1115/1.3640546
16. Budiansky B, Rice JR (1973) Conservation laws and Energy-Release rates. J Appl Mech 40:201–203. https://doi.org/10.1115/1.3422926
17. Knowles JK, Sternberg E (1972) On a class of conservation laws in linearized and finite elastostatics. Arch Ration Mech Anal 44:187–211. https://doi.org/10.1007/BF00250778
18. Rice JR (1972) Some remarks on elastic crack-tip stress fields. Int J Solids Struct 8:751–758. https://doi.org/10.1016/0020-7683(72)90040-6
19. Guo Y, Li Q (2017) Material configurational forces applied to mixed mode crack propagation. Theoret Appl Fract Mech 89:147–157. https://doi.org/10.1016/j.tafmec.2017.02.006
20. Li Q, Lv JN (2017) Invariant integrals of crack interaction with an inhomogeneity. Eng Fract Mech 171:76–84. https://doi.org/10.1016/j.engfracmech.2016.12.013
21. Zhou R, Coombs WM, Xu Y, Zhang P, Wang LG (2022) A configurational force-based material point method for crack propagation modelling in 2D. Theoret Appl Fract Mech 117:103186. https://doi.org/10.1016/j.tafmec.2021.103186
22. Frankl SM, Pletz M, Schuecker C (2022) Improved concept for iterative crack propagation using configurational forces for targeted angle correction. Eng Fract Mech 266:108403. https://doi.org/10.1016/j.engfracmech.2022.108403
23. Ai W, Bird RE, Coombs WM, Augarde CE (2019) A configurational force driven cracking particle method for modelling crack propagation in 2D. Eng Anal Bound Elem 104:197–208. https://doi.org/10.1016/j.enganabound.2019.03.008
24. Chang JH, Wu WH (2011) Using M-integral for multi-cracked problems subjected to nonconservative and nonuniform crack surface tractions. Int J Solids Struct 48:2605–2613. https://doi.org/10.1016/j.ijsolstr.2011.05.005
25. Kim S, Kim H, Kim SY (2021) Configurational force on a dynamic dislocation with localized Oscillation. Int J Plast 136:102814. https://doi.org/10.1016/j.ijplas.2020.102814
26. Baxevanakis KP, Giannakopoulos AE (2015) Finite element analysis of discrete edge dislocations: configurational forces and conserved integrals. Int J Solids Struct 62:52–65. https://doi.org/10.1016/J.IJSOLSTR.2015.01.025
27. Eshelby JD, Peierls RE (1957) The determination of the elastic field of an ellipsoidal inclusion, and related problems. Proc R Soc Lond Math Phys Sci 241:376–396. https://doi.org/10.1098/rspa.1957.0133
28. Koko A, Elmukashfi E, Becker TH, Karamched PS, Wilkinson AJ, Marrow TJ (2022) In situ characterisation of the strain fields of intragranular slip bands in ferrite by high-resolution electron backscatter diffraction. Acta Mater 239:118284. https://doi.org/10.1016/j.actamat.2022.118284
29. Lazar M, Kirchner HOK (2007) The Eshelby stress tensor, angular momentum tensor and dilatation flux in gradient elasticity. Int J Solids Struct 44:2477–2486. https://doi.org/10.1016/j.ijsolstr.2006.07.018

30. Agiasofitou E, Lazar M (2017) Micromechanics of dislocations in solids: J -, M -, and L -integrals and their fundamental relations. Int J Eng Sci 114:16–40. https://doi.org/10.1016/j.ijengsci.2017.02.001
31. Lazar M, Agiasofitou EJ- (2023) L-integrals of line charges and line forces. Acta Mech 234:3131–3159. https://doi.org/10.1007/s00707-023-03540-3
32. Richard HA, Schramm B, Schirmeisen NH (2014) Cracks on mixed mode loading - Theories, experiments, simulations. Int J Fatigue 62:93–103. https://doi.org/10.1016/j.ijfatigue.2013.06.019
33. ASTM E1820-18 Test Method for Measurement of Fracture Toughness 2025. https://doi.org/10.1520/E1820-25
34. D6671M A (2006) Standard test method for mixed mode I-Mode II interlaminar fracture toughness of unidirectional fiber reinforced polymer matrix composites. ASTM Int :15
35. Malekan M, Khosravi A, St-Pierre L (2022) An Abaqus plug-in to simulate fatigue crack growth. Eng Comput 38:2991–3005. https://doi.org/10.1007/s00366-021-01321-x
36. Nesládek M, Španiel M (2017) An Abaqus plugin for fatigue predictions. Adv Eng Softw 103:1–11. https://doi.org/10.1016/j.advengsoft.2016.10.008
37. Moutou Pitti R, Badulescu C, Grédiac M (2014) Characterization of a cracked specimen with full-field measurements: direct determination of the crack tip and energy release rate calculation. Int J Fract 187:109–121. https://doi.org/10.1007/s10704-013-9921-5
38. Meindlhumer M, Alfreider M, Sheshi N, Hohenwarter A, Todt J, Rosenthal M et al (2025) Resolving the fundamentals of the J-integral concept by multi-method in situ nanoscale stress-strain mapping. Commun Mater 6:35. https://doi.org/10.1038/s43246-025-00752-z
39. Hufnagel TC, Vempati UK, Almer JD (2013) Crack-Tip strain field mapping and the toughness of metallic glasses. PLoS ONE 8:e83289. https://doi.org/10.1371/journal.pone.0083289
40. Marshall DB, Lawn BR (1979) Residual stress effects in Sharp contact cracking. J Mater Sci 1979 14:8. https://doi.org/10.1007/BF00551043
41. Lei Y, O'Dowd NP, Webster GA (2000) Fracture mechanics analysis of a crack in a residual stress field. Int J Fract 106:195–216. https://doi.org/10.1023/A:1026574400858
42. Yin Y, Xie H, He W (2020) In situ SEM-DIC technique and its application to characterize the high-temperature fatigue crack closure effect. Sci China Technol Sci 63:265–276. https://doi.org/10.1007/s11431-018-9477-6
43. Fry AT, Lodeiro MJ, Koko A, Booth-Downs F, Crocker LE (2023) Effect of specimen misalignment in static and fatigue testing of small-scale test pieces. Teddington, UK: https://doi.org/10.47120/npl.MAT122
44. Christ B, Swanson S (1976) Alignment problems in the tensile test. J Test Eval 4:405–417. https://doi.org/10.1520/JTE11371J
45. Wilkinson AJ, Meaden G, Dingley DJ (2006) High-resolution elastic strain measurement from electron backscatter diffraction patterns: new levels of sensitivity. Ultramicroscopy 106:307–313. https://doi.org/10.1016/j.ultramic.2005.10.001
46. Troost KZ, van der Sluis P, Gravesteijn DJ (1993) Microscale elastic-strain determination by backscatter Kikuchi diffraction in the scanning electron microscope. Appl Phys Lett 62:1110–1112. https://doi.org/10.1063/1.108758
47. Schreier H, Orteu J-J, Sutton MA (2009) Image correlation for Shape, motion and deformation measurements. Springer US, Boston, MA. https://doi.org/10.1007/978-0-387-78747-3
48. Di Gioacchino F, Quinta da Fonseca J (2013) Plastic strain mapping with Sub-micron resolution using digital image correlation. Exp Mech 53:743–754. https://doi.org/10.1007/s11340-012-9685-2
49. Sanders JL (1960) On the Griffith-Irwin fracture theory. J Appl Mech 27:352–353. https://doi.org/10.1115/1.3643965
50. Cherepanov GP (1967) Crack propagation in continuous media. J Appl Math Mech 31:503–512. https://doi.org/10.1016/0021-8928(67)90034-2
51. Hutchinson JW (1968) Singular behaviour at the end of a tensile crack in a hardening material. J Mech Phys Solids 16:13–31. https://doi.org/10.1016/0022-5096(68)90014-8
52. Rice JR, Rosengren GF (1968) Plane strain deformation near a crack tip in a power-law hardening material. J Mech Phys Solids 16:1–12. https://doi.org/10.1016/0022-5096(68)90013-6
53. Shih CF, Asaro RJ (1988) Elastic-Plastic analysis of cracks on bimaterial interfaces: part I—Small scale yielding. J Appl Mech 55:299–316. https://doi.org/10.1115/1.3173676
54. Li FZ, Shih CF, Needleman A (1985) A comparison of methods for calculating energy release rates. Eng Fract Mech 21:405–421. https://doi.org/10.1016/0013-7944(85)90029-3
55. Shih CF (1981) Relationships between the J-integral and the crack opening displacement for stationary and extending cracks. J Mech Phys Solids 29:305–326. https://doi.org/10.1016/0022-5096(81)90003-X
56. Karlsson A, Bäcklund J (1978) J-integral at loaded crack surfaces. Int J Fract 14:R311–R318. https://doi.org/10.1007/BF00116006
57. Walters MC, Paulino GH, Dodds RH (2005) Interaction integral procedures for 3-D curved cracks including surface tractions. Eng Fract Mech 72:1635–1663. https://doi.org/10.1016/j.engfracmech.2005.01.002
58. Kim KCA (2008) Interaction integrals for thermal fracture of functionally graded materials. Eng Fract Mech 75:2542–2565. https://doi.org/10.1016/j.engfracmech.2007.07.011
59. Shih CF, Moran B, Nakamura T (1986) Energy release rate along a three-dimensional crack front in a thermally stressed body. Int J Fract 30:79–102. https://doi.org/10.1007/BF00034019
60. Haftbaradaran H, Qu J (2014) A path-independent integral for fracture of solids under combined electrochemical and mechanical loadings. J Mech Phys Solids 71:1–14. https://doi.org/10.1016/j.jmps.2014.06.007
61. Ming-Yuan H, Hutchinson JW (1989) Crack Deflection at an interface between dissimilar elastic materials. Int J Solids Struct 25:1053–1067. https://doi.org/10.1016/0020-7683(89)90021-8
62. Yu H, Wu L, Guo L, He Q, Du S (2010) Interaction integral method for the interfacial fracture problems of two nonhomogeneous materials. Mech Mater 42:435–450. https://doi.org/10.1016/j.mechmat.2010.01.001
63. Yu H, Wu L, Guo L, Du S, He Q (2009) Investigation of mixed-mode stress intensity factors for nonhomogeneous materials using an interaction integral method. Int J Solids Struct 46:3710–3724. https://doi.org/10.1016/j.ijsolstr.2009.06.019
64. Dowling N, Begley J (1976) Fatigue Crack Growth During Gross Plasticity and the J-Integral. Mechanics of Crack Growth, ASTM International100 Barr Harbor Drive, PO Box C700, West Conshohocken, PA 19428–2959; pp. 82–103. https://doi.org/10.1520/STP33940S
65. Smelser RE, Gurtin ME (1977) On the J-integral for Bi-material bodies. Int J Fract 13:382–384. https://doi.org/10.1007/BF00040155
66. Kim H, Kim S, Kim SY (2021) Lattice-based J integral for a steadily moving dislocation. Int J Plast 138:102949. https://doi.org/10.1016/j.ijplas.2021.102949
67. Markenscoff X, Ni L (2010) The energy-release rate and self-force of dynamically expanding spherical and plane inclusion boundaries with dilatational eigenstrain. J Mech Phys Solids 58:1–11. https://doi.org/10.1016/j.jmps.2009.10.001

68. Eshelby JD (1956) In: Seitz F, Turnbull DBT-SSP (eds) The continuum theory of lattice defects, vol 3. Academic, pp 79–144. https://doi.org/10.1016/S0081-1947(08)60132-0.
69. Eshelby JD (1951) The force on an elastic singularity. Philosophical transactions of the Royal society of London series A. Math Phys Sci 244:87–112. https://doi.org/10.1098/rsta.1951.0016
70. Shivakumar KN, Raju IS (1992) An equivalent domain integral method for three-dimensional mixed-mode fracture problems. Eng Fract Mech 42:935–959. https://doi.org/10.1016/0013-7944(92)90134-Z
71. Moran B, Shih CF (1987) Crack tip and associated domain integrals from momentum and energy balance. Eng Fract Mech 27:615–642. https://doi.org/10.1016/0013-7944(87)90155-X
72. Nikishkov GP, Atluri SN (1987) Calculation of fracture mechanics parameters for an arbitrary three-dimensional crack, by the 'equivalent domain integral' method. Int J Numer Methods Eng 24:1801–1821. https://doi.org/10.1002/nme.1620240914
73. Parks DM (1977) The virtual crack extension method for nonlinear material behavior. Comput Methods Appl Mech Eng 12:353–364. https://doi.org/10.1016/0045-7825(77)90023-8
74. Nikishkov GP, Vershinin AV, Nikishkov YG (2016) Mesh-independent equivalent domain integral method for J-integral evaluation. Adv Eng Softw 100:308–318. https://doi.org/10.1016/j.advengsoft.2016.08.006
75. Hussain MA, Pu SL, Underwood J (1974) Strain Energy Release Rate for a Crack Under Combined Mode I and Mode II. In: Irwin GR, editor. Fracture Analysis: Proceedings of the 1973 National Symposium on Fracture Mechanics, Part II, West Conshohocken, PA: ASTM International; pp. 2–28. https://doi.org/10.1520/STP33130S
76. Chang JH, Chien AJ (2002) Evaluation of M-integral for anisotropic elastic media with multiple defects. Int J Fract 114:267–289. https://doi.org/10.1023/A:1015561313059
77. Chen Y-H (2002) Advances in conservation laws and energy release rates. Springer Netherlands, Dordrecht. https://doi.org/10.1007/978-94-015-9908-5
78. Chen Y-H, Lu TJ (2003) Recent developments and applications of invariant integrals. Appl Mech Rev 56:515–552. https://doi.org/10.1115/1.1582199
79. Koko A, Elmukashfi E, Dragnevski K, Wilkinson AJ, Marrow TJ (2021) J-integral analysis of the elastic strain fields of ferrite deformation twins using electron backscatter diffraction. Acta Mater 218:117203. https://doi.org/10.1016/j.actamat.2021.117203
80. Huber O, Nickel J, Kuhn G (1993) On the decomposition of the J-integral for 3D crack problems. Int J Fract 64:339–348. https://doi.org/10.1007/BF00017849
81. Rigby RH, Aliabadi MH (1993) Mixed-mode J-integral method for analysis of 3D fracture problems using BEM. Eng Anal Bound Elem 11:239–256. https://doi.org/10.1016/0955-7997(93)90026-H
82. Shi Q, Plancher E, Loisnard D, Karamched P, Liu J, Chen Z et al Improved high-resolution EBSD analyses by correcting radial distortion of electron diffraction patterns. Mater Charact 2022;194. https://doi.org/10.1016/j.matchar.2022.112458
83. HARDIN TJ, RUGGLES TJ, KOCH DP, NIEZGODA SR, FULLWOOD DT, HOMER ER (2015) Analysis of traction-free assumption in high-resolution EBSD measurements. J Microsc 260:73–85. https://doi.org/10.1111/jmi.12268
84. Koko A, Tong V, Wilkinson AJ, Marrow TJ An iterative method for reference pattern selection in high-resolution electron backscatter diffraction (HR-EBSD). Ultramicroscopy 2023;248. https://doi.org/10.1016/j.ultramic.2023.113705
85. Siebert T, Hack E, Lampeas G, Patterson EA, Splitthof K (2021) Uncertainty quantification for DIC displacement measurements in industrial environments. Exp Tech 45:685–694. https://doi.org/10.1007/s40799-021-00447-3
86. Zhao J, Pan B (2023) Uncertainty quantification for 3D digital image correlation displacement measurements using Monte Carlo method. Opt Lasers Eng 170:107777. https://doi.org/10.1016/j.optlaseng.2023.107777
87. Jose K, Meng Z, Dennis AR, Grega I, Shaikeea AJD, Deshpande VS (2025) Exploration of digital volume correlation in nominally homogeneous metals. Mech Mater 207:105394. https://doi.org/10.1016/j.mechmat.2025.105394
88. Buljac A, Taillandier-Thomas T, Helfen L, Morgeneyer TF, Hild F (2018) Evaluation of measurement uncertainties of digital volume correlation applied to laminography data. J Strain Anal Eng Des 53:49–65. https://doi.org/10.1177/0309324717748097
89. Paraskevoulakos C, Kunther W, Michel A (2024) Quantifying the effect of scanning parameters on digital volume correlation analysis for in situ X-ray imaging of concrete. Constr Build Mater 449:138408. https://doi.org/10.1016/j.conbuildmat.2024.138408
90. Luan X, Qin H, Liu F, Dai Z, Yi Y, Li Q (2018) The mechanical properties and elastic anisotropies of cubic Ni3Al from first principles calculations. Cryst (Basel) 8. https://doi.org/10.3390/cryst8080307
91. Sutton MA, Yan JH, Tiwari V, Schreier HW, Orteu JJ (2008) The effect of out-of-plane motion on 2D and 3D digital image correlation measurements. Opt Lasers Eng 46:746–757. https://doi.org/10.1016/j.optlaseng.2008.05.005
92. Bay BK, Smith TS, Fyhrie DP, Saad M (1999) Digital volume correlation: Three-dimensional strain mapping using X-ray tomography. Exp Mech 39:217–226. https://doi.org/10.1007/BF02323555
93. Becker TH Extracting fracture properties from digital image and volume correlation displacement data: A review. Strain 2023. https://doi.org/10.1111/str.12469
94. Liu H, Hild F (2024) Quantifying 3D crack propagation in nodular graphite cast iron using advanced digital volume correlation and X-ray computed tomography. Eng Fract Mech 296:109824. https://doi.org/10.1016/J.ENGFRACMECH.2023.109824
95. Britton TB, Wilkinson AJ (2012) High resolution electron backscatter diffraction measurements of elastic strain variations in the presence of larger lattice rotations. Ultramicroscopy 114:82–95. https://doi.org/10.1016/j.ultramic.2012.01.004
96. Wilkinson AJ, Meaden G, Dingley DJ (2006) High resolution mapping of strains and rotations using electron backscatter diffraction. Mater Sci Technol 22:1271–1278. https://doi.org/10.1179/174328406X130966
97. Yang W, Larson BC, Tischler JZ, Ice GE, Budai JD, Liu W (2004) Differential-aperture X-ray structural microscopy: a submicron-resolution three-dimensional probe of local microstructure and strain. Micron 35:431–439. https://doi.org/10.1016/j.micron.2004.02.004
98. Ramberg W, Osgood WR (1943) Description of Stress-strain Curves by Three Parameters. Washington DC
99. Schreier HW, Sutton MA (2002) Systematic errors in digital image correlation due to undermatched subset shape functions. Exp Mech 42:303–310. https://doi.org/10.1007/BF02410987
100. Schreier HW (2000) Systematic errors in digital image correlation caused by intensity interpolation. Opt Eng 39:2915. https://doi.org/10.1117/1.1314593
101. Shi MX, Huang Y, Gao H (2004) The J-integral and geometrically necessary dislocations in nonuniform plastic deformation. Int J Plast 20:1739–1762. https://doi.org/10.1016/J.IJPLAS.2003.11.013
102. Kuang JH, Chen YC (1996) The values of J-integral within the plastic zone. Eng Fract Mech 55:869–881. https://doi.org/10.1016/S0013-7944(96)00077-X

103. Ma L, Lu TJ, Korsunsky AM (2006) Vector j-integral analysis of crack interaction with pre-existing singularities. J Appl Mech Trans ASME 73:876–883. https://doi.org/10.1115/1.2165243
104. Mohammadi S (2008) Extended finite element method. Blackwell Publishing Ltd, Oxford, UK. https://doi.org/10.1002/9780470697795
105. Sha GT, Chien-Tung Y (1985) Weight function calculations for mixedmode fracture problems with the virtual crack extension technique. Eng Fract Mech 21:1119–1149. https://doi.org/10.1016/0013-7944(85)90173-0
106. Strohmann T, Starostin-Penner D, Breitbarth E, Requena G (2021) Automatic detection of fatigue crack paths using digital image correlation and convolutional neural networks. Fatigue Fract Eng Mater Struct 44:1336–1348. https://doi.org/10.1111/ffe.13433
107. Gehri N, Mata-Falcón J, Kaufmann W (2020) Automated crack detection and measurement based on digital image correlation. Constr Build Mater 256:119383. https://doi.org/10.1016/j.conbuildmat.2020.119383
108. Cinar AF, Barhli SM, Hollis D, Flansbjer M, Tomlinson RA, Marrow TJ et al (2017) An autonomous surface discontinuity detection and quantification method by digital image correlation and phase congruency. Opt Lasers Eng 96:94–106. https://doi.org/10.1016/J.OPTLASENG.2017.04.010
109. Zhang K, Zhang K, Liu W, Xie J (2023) A novel DIC-based methodology for crack identification in a jointed rock mass. Mater Des 230:111944. https://doi.org/10.1016/j.matdes.2023.111944
110. Anderson TL (2017) Elastic-Plastic fracture Mechanics. fracture Mechanics - Fundamentals and applications, 4th edn. CRC, p 688. https://doi.org/10.1201/9781315370293
111. Rodella J, Dhondt G, Köster P, Sander M, Piorun S (2021) Determination of the crack propagation direction in Mixed-Mode missions due to Cyclic loading. Appl Sci 11:1673. https://doi.org/10.3390/app11041673
112. Rozumek D, Macha E (2009) A survey of failure criteria and parameters in mixed-mode fatigue crack growth. Mater Sci 45:190–210. https://doi.org/10.1007/s11003-009-9179-2
113. Wang Y, Wang W, Zhang B, Li C-Q (2020) A review on mixed mode fracture of metals. Eng Fract Mech 235:107126. https://doi.org/10.1016/j.engfracmech.2020.107126
114. Qian J, Fatemi A (1996) Mixed mode fatigue crack growth: A literature survey. Eng Fract Mech 55:969–990. https://doi.org/10.1016/S0013-7944(96)00071-9
115. Tuna M, Trovalusci P, Fantuzzi N (2025) An energy-based fracture criterion for quasi-brittle crack propagation in micropolar continuum: analytical and numerical study. Int J Eng Sci 206:104173. https://doi.org/10.1016/j.ijengsci.2024.104173
116. Korsunsky AM, Dini D, Dunne FPE, Walsh MJ (2007) Comparative assessment of dissipated energy and other fatigue criteria. Int J Fatigue 29:1990–1995. https://doi.org/10.1016/J.IJFATIGUE.2007.01.007
117. Erdogan F, Sih GC (1963) On the crack extension in plates under plane loading and transverse shear. J Basic Eng 85:519–525. https://doi.org/10.1115/1.3656897
118. Cotterell B, Rice JR (1980) Slightly curved or kinked cracks. Int J Fract 16:155–169. https://doi.org/10.1007/BF00012619
119. Leide AJ, Todd RI, Armstrong DEJ (2021) Effect of ion irradiation on nanoindentation fracture and deformation in silicon carbide. JOM 73:1617–1628. https://doi.org/10.1007/s11837-021-04636-8
120. Yoffe EH (1982) Elastic stress fields caused by indenting brittle materials. Philos Mag A 46:617–628. https://doi.org/10.1080/01418618208236917
121. Anstis GR, Chantikul P, Lawn BR, Marshall DB (1981) A critical evaluation of indentation techniques for measuring fracture toughness: I, direct crack measurements. J Am Ceram Soc 64:533–538. https://doi.org/10.1111/j.1151-2916.1981.tb10320.x
122. Marshall DB, Lawn BR, Evans AG (1982) Elastic/Plastic indentation damage in ceramics: the lateral crack system. J Am Ceram Soc 65:561–566. https://doi.org/10.1111/J.1151-2916.1982.TB10782.X
123. Koko A, Becker TH, Elmukashfi E, Pugno NM, Wilkinson AJ, Marrow TJ (2023) HR-EBSD analysis of in situ stable crack growth at the micron scale. J Mech Phys Solids 172:105173. https://doi.org/10.1016/j.jmps.2022.105173
124. Ishida T, Kakushima K, Mizoguchi T, Fujita H (2012) Role of dislocation movement in the electrical conductance of nanocontacts. Sci Rep 2:623. https://doi.org/10.1038/srep00623
125. Zhuo F, Zhou X, Gao S, Höfling M, Dietrich F, Groszewicz PB et al (2022) Anisotropic dislocation-domain wall interactions in ferroelectrics. Nat Commun 13:6676. https://doi.org/10.1038/s41467-022-34304-7
126. Liu W, Yu L, Liu Y, Sui H, Fan H, Duan H (2022) Dislocation pile-up polarization model for mechanical properties of polycrystalline metals based on grain boundary resistance variability. J Mech Phys Solids 160:104793. https://doi.org/10.1016/j.jmps.2022.104793
127. Lekhnitskii SG (1981) General equations of the theory of elasticity of an anisotropic body. theory of elasticity of an anisotropic elastic body, 1st edn. MIR, Moscow, pp 15–73
128. Yu H, Liu J, Karamched P, Wilkinson AJ, Hofmann F (2019) Mapping the full lattice strain tensor of a single dislocation by high angular resolution transmission Kikuchi diffraction (HR-TKD). Scr Mater 164:36–41. https://doi.org/10.1016/j.scriptamat.2018.12.039
129. Yoffe EH (1961) A dislocation at a free surface. Phil Mag 6:1147–1155. https://doi.org/10.1080/14786436108239675
130. Bond WL (1943) The mathematics of the physical properties of crystals. Bell Syst Tech J 22:1–72. https://doi.org/10.1002/j.1538-7305.1943.tb01304.x
131. Salvati E, Sui T, Korsunsky AM (2016) Uncertainty quantification of residual stress evaluation by the FIB–DIC ring-core method due to elastic anisotropy effects. Int J Solids Struct 87:61–69. https://doi.org/10.1016/j.ijsolstr.2016.02.031
132. Tong V, Jiang J, Wilkinson AJ, Britton T, Ben (2015) The effect of pattern overlap on the accuracy of high resolution electron backscatter diffraction measurements. Ultramicroscopy 155:62–73. https://doi.org/10.1016/j.ultramic.2015.04.019
133. Koko A, Singh S, Barhli S, Connolley T, Vo NT, Wigger T et al (2023) 3-Dimensional analysis of fatigue crack fields and crack growth by in situ synchrotron X-ray tomography. Int J Fatigue 170:107541. https://doi.org/10.1016/j.ijfatigue.2023.107541
134. Mostafavi M, Collins DM, Cai B, Bradley R, Atwood RC, Reinhard C et al (2015) Yield behavior beneath hardness indentations in ductile metals, measured by three-dimensional computed X-ray tomography and digital volume correlation. Acta Mater 82:468–482. https://doi.org/10.1016/j.actamat.2014.08.046
135. Tomičević Z, Kodvanj J, Hild F (2016) Characterization of the nonlinear behavior of nodular graphite cast iron via inverse identification–Analysis of uniaxial tests. Eur J Mech A Solids 59:140–154. https://doi.org/10.1016/j.euromechsol.2016.02.010
136. Lachambre J, Réthoré J, Weck A, Buffiere J-Y (2015) Extraction of stress intensity factors for 3D small fatigue cracks using digital volume correlation and X-ray tomography. Int J Fatigue 71:3–10. https://doi.org/10.1016/j.ijfatigue.2014.03.022
137. Molteno MR (2017) Measuring fracture properties using digital image and volume correlation: decomposing the J-integral for mixed-mode parameters. Doctor of Philosophy. Stellenbosch University

138. Zhou H, Lebensohn RA, Reischig P, Ludwig W, Bhattacharya K (2022) Imposing equilibrium on experimental 3-D stress fields using Hodge decomposition and FFT-based optimization. Mech Mater 164:104109. https://doi.org/10.1016/j.mechmat.2021.104109
139. Lawn B, Wilshaw R (1975) Indentation fracture: principles and applications. J Mater Sci 10:1049–1081. https://doi.org/10.1007/BF00823224
140. Cook RF, Gerbig Y, Schoenmaker J, Stranick S (2009) Stress-intensity factor and toughness measurement at the nanoscale using confocal Raman microscopy. 12th International Conference on Fracture 2009, ICF-12. ;5:3758–66
141. Lawn B, Wilshaw R (1975) Indentation fracture: principles and applications. J Mater Sci 1975 10:6. https://doi.org/10.1007/BF00823224
142. Evans AG, Charles EA (1976) Fracture toughness determinations by indentation. J Am Ceram Soc 59:371–372. https://doi.org/10.1111/J.1151-2916.1976.TB10991.X
143. Lawn BR, Evans AG, Marshall DB (1980) Elastic/Plastic indentation damage in ceramics: the Median/Radial crack system. J Am Ceram Soc 63:574–581. https://doi.org/10.1111/j.1151-2916.1980.tb10768.x
144. Dukino RD, Swain MV (1992) Comparative measurement of indentation fracture toughness with Berkovich and Vickers indenters. J Am Ceram Soc 75:3299–3304. https://doi.org/10.1111/j.1151-2916.1992.tb04425.x
145. Morrell BREBLLR (2008) Measurement Good Practice Guide No 9: Palmqvist Toughness for Hard and Brittle Materials. Teddington
146. Quinn GD, Bradt RC (2007) On the Vickers indentation fracture toughness test. J Am Ceram Soc 90:673–680. https://doi.org/10.1111/J.1551-2916.2006.01482.X
147. Jiapeng S, Cheng L, Han J, Ma A, Fang L (2017) Nanoindentation induced deformation and Pop-in events in a silicon crystal: molecular dynamics simulation and experiment. Sci Rep 7:10282. https://doi.org/10.1038/s41598-017-11130-2
148. Goel S, Haque Faisal N, Luo X, Yan J, Agrawal A (2014) Nanoindentation of polysilicon and single crystal silicon: molecular dynamics simulation and experimental validation. J Phys D Appl Phys 47:275304. https://doi.org/10.1088/0022-3727/47/27/275304
149. Tanaka M, Higashida K, Nakashima H, Takagi H, Fujiwara M (2006) Orientation dependence of fracture toughness measured by indentation methods and its relation to surface energy in single crystal silicon. Int J Fract 2006 139:3. https://doi.org/10.1007/S10704-006-0021-7
150. Qin J, Huang Y, Hwang KC, Song J, Pharr GM (2007) The effect of indenter angle on the microindentation hardness. Acta Mater 55:6127–6132. https://doi.org/10.1016/J.ACTAMAT.2007.07.016
151. Britton TB, Liang H, Dunne FPE, Wilkinson AJ (2010) The effect of crystal orientation on the indentation response of commercially pure titanium: experiments and simulations. Proc Royal Soc A: Math Phys Eng Sci 466:695–719. https://doi.org/10.1098/RSPA.2009.0455
152. Liu M, Lin JY, Lu C, Tieu KA, Zhou K, Koseki T (2017) Progress in Indentation Study of Materials via Both Experimental and Numerical Methods. Crystals 2017, Vol 7, Page 258. ;7:258. https://doi.org/10.3390/CRYST7100258
153. Moreno-Mateos MA, Steinmann P (2024) Configurational force method enables fracture assessment in soft materials. J Mech Phys Solids 186:105602. https://doi.org/10.1016/j.jmps.2024.105602
154. Li X, Ding Z, Liu C, Bao S, Gao Z (2020) Evaluation and comparison of fracture toughness for metallic materials in different conditions by ASTM and ISO standards. Int J Press Vessels Pip 187:104189. https://doi.org/10.1016/J.IJPVP.2020.104189
155. GUAN P. Study and comparison of test method for measurement of fracture toughness between ASTM and ISO standards. J Mech Eng (2017) ;53:60. https://doi.org/10.3901/JME.2017.06.060
156. MacDowell AA, Celestre RS, Tamura N, Spolenak R, Valek B, Brown WL et al (2001) Submicron X-ray diffraction. Nucl Instrum Methods Phys Res A 467–468:936–943. https://doi.org/10.1016/S0168-9002(01)00530-7
157. Lorentzen T, Leffers T (1992) Strain tensor measurements by neutron diffraction. Measurement of residual and applied stress using neutron diffraction. Springer Netherlands, Dordrecht, pp 253–261. https://doi.org/10.1007/978-94-011-2797-4_16
158. Koko A, Marrow J, Elmukashfi E (2021) A computational method for the determination of the elastic displacement field using measured elastic deformation field. Appear :5
159. Pierron F, Grédiac M Towards material testing 2.0. A review of test design for identification of constitutive parameters from full-field measurements. Strain 2021;57. https://doi.org/10.1111/str.12370
160. Griffith AA (1921) VI. The phenomena of rupture and flow in solids. Philosophical transactions of the Royal society of London series A, containing papers of a mathematical or. Phys Character 221 163 LP – 198. https://doi.org/10.1098/rsta.1921.0006
161. Hashin Z, Shtrikman S (1963) A variational approach to the theory of the elastic behaviour of multiphase materials. J Mech Phys Solids 11:127–140. https://doi.org/10.1016/0022-5096(63)90060-7
162. Purushottam Raj Purohit RRP, Richeton T, Berbenni S, Germain L, Gey N, Connolley T et al (2021) Estimating single-crystal elastic constants of polycrystalline β metastable titanium alloy: A bayesian inference analysis based on high energy X-ray diffraction and micromechanical modeling. Acta Mater 208:116762. https://doi.org/10.1016/j.actamat.2021.116762